Variational multiscale large eddy simulation of turbulent flow in a planar asymmetric diffuser

By   V. Gravemeier†

1. Motivation and objectives

Two important aspects characterize variational multiscale large eddy simulation (LES). Firstly, a variational projection separates scale ranges within the variational multiscale LES, rather than a spatial filter as in traditional LES. Secondly, the (direct) influence of the subgrid-scale model, which is introduced to represent the effect of the unresolved scales on the resolved scales, is confined to the small resolved scales. Thus, the larger scales are solved as a direct numerical simulation (DNS), that is, without any (direct) influence of the modeling term. Of course, the large resolved scales are still indirectly influenced by the subgrid-scale model due to the inherent coupling of all scales. The initial publication on the variational multiscale LES by Hughes *et al.* (2000) and a recent review article by Gravemeier (2005b) provide a detailed description of this phenomenon. Various test cases have been studied to investigate the performance of the variational multiscale method in practical applications, and generally good results have been reported. However, most of these studies have been within simpler configurations. A brief overview of the flow problems addressed so far, along with the respectively applied numerical methods and the respective approach for separating the scale groups, can be found in Gravemeier (2005b).

In the present study, the variational multiscale LES is applied to turbulent flow in a planar asymmetric diffuser. The Reynolds number of the investigated flow is about 10,000, based on the half-width of the inlet channel and the streamwise bulk mean velocity. Several features of turbulent flow in a diffuser indicate its higher complexity. These include most notably:

• A large unsteady separation bubble that is due to an adverse pressure gradient and that emerges about halfway down the lower deflected wall. The flow reattaches within the outlet channel.

• A sudden change in the streamwise pressure gradient from slightly favorable to strongly adverse at the diffuser throat and a subsequent gradual decrease to weakly adverse.

• A slowly growing internal layer that emerges at the upper flat wall in the relaxation zone downstream of the sharp variation in the streamwise pressure gradient, according to the recent numerical study in Wu *et al.* (2006).

Experimental studies of turbulent flow in a planar asymmetric diffuser have been presented in Buice & Eaton (1997) and in Obi *et al.* (1993). A DNS of the flow at this Reynolds number in the present diffuser configuration is still prohibitively expensive. Large eddy simulations have been conducted by Kaltenbach *et al.* (1999) and recently by Wu *et al.* (2006). The diffuser problem was also a test case at a workshop in 1999; see Hellsten & Rautaheimo (1999). The selection was due in part to the difficulty of

† Current address: Technical University of Munich, Chair for Computational Mechanics, Boltzmannstr. 15, D-85747 Garching, Germany. E-mail: vgravem@lnm.mw.tum.de

accurately predicting the point of separation and the extent of the recirculation region. These observations also suggest that the diffuser configuration would be a challenging test case for evaluating the variational multiscale LES in the present study. A detailed version of the present study can be found in Gravemeier (2005c).

The predecessor of the present work is the study in Gravemeier (2005a). In that study, a class of scale-separating operators based on multigrid operators was proposed and analyzed. The scale-separating operators were consistently used for both the extraction of the small scales, to which the subgrid-scale model is applied, and any scale separation necessary for a dynamic modeling procedure. All scale-separating operators were implemented in the CDP-α code, the flagship LES code of the Center for Turbulence Research; see, for example, Ham *et al.* (2003) for some features of this code. Underlying this code is a second-order energy-conserving finite volume method particularly suited for applications on unstructured colocated grids. A comparison of two representatives of the proposed class of multigrid scale-separating operators with discrete smooth filters revealed its superiority, both in terms of quality of results and required computational effort. This superiority was particularly significant for one of these two scale-separating operators. This particular operator was shown to provide a projective scale separation in Gravemeier (2005a), and it is essentially the same operator as the one proposed in Koobus & Farhat (2004).

2. Variational finite volume formulation

A weighted residual formulation of the Navier-Stokes equations is given as follows: find $\{\mathbf{u}, p\} \in \mathcal{S}_{\mathbf{u}p}$, such that

$$B_{\text{NS}}(\mathbf{v}, q; \mathbf{u}, p) = (\mathbf{v}, \mathbf{f})_{\Omega} \qquad \forall \{\mathbf{v}, q\} \in \mathcal{V}_{\mathbf{u}p}, \tag{2.1}$$

where $\mathbf{v}$ and q denote the weighting functions. $\mathcal{S}_{\mathbf{u}p}$ and $\mathcal{V}_{\mathbf{u}p}$ represent the combined formulation of the solution and weighting function spaces for velocity and pressure: $\mathcal{S}_{\mathbf{u}p} := \mathcal{S}_{\mathbf{u}} \times \mathcal{S}_p$ and $\mathcal{V}_{\mathbf{u}p} := \mathcal{V}_{\mathbf{u}} \times \mathcal{V}_p$. The form $B_{\text{NS}}(\mathbf{v}, q; \mathbf{u}, p)$ on the left hand side of (2.1), which is linear on the first slot (i.e. $\mathbf{v}$, q) and non-linear on the second slot (i.e. $\mathbf{u}$, p), is defined as

$$B_{\text{NS}}(\mathbf{v}, q; \mathbf{u}, p) = \left(\mathbf{v}, \frac{\partial \mathbf{u}}{\partial t}\right)_{\Omega} + (\mathbf{v}, \nabla \cdot (\mathbf{u} \otimes \mathbf{u}))_{\Omega} + (\mathbf{v}, \nabla p)_{\Omega} - (\mathbf{v}, \nabla \cdot (2\nu \varepsilon(\mathbf{u})))_{\Omega}$$
$$+ (q, \nabla \cdot \mathbf{u})_{\Omega}. \tag{2.2}$$

The domain Ω is now discretized into n control volumes Ω_i $(i = 1, ..., n)$, with control volume boundaries Γ_i. The weighting functions are chosen to be

$$\mathbf{v}^h = \sum_i \mathbf{v}_i^h, \quad q^h = \sum_i q_i^h, \tag{2.3}$$

where

$$\mathbf{v}_i^h = \mathbf{1}, \quad q_i^h = 1 \quad \text{in} \quad \Omega_i \tag{2.4}$$

and zero elsewhere. In (2.4), $\mathbf{1}$ explicitly means that each component of $\mathbf{v}_i^h$ is of unit value. The characteristic control volume length of the discretization is h. With these definitions at hand, the weighted residual equation (2.1) may be reformulated as a variational finite volume equation for each $\mathbf{v}_i^h$ and q_i^h: find $\{\mathbf{u}^h, p^h\} \in \mathcal{S}_{\mathbf{u}p}^h$, such that

$$B_{\text{NS}}^{\text{FV}}(\mathbf{v}_i^h, q_i^h; \mathbf{u}^h, p^h) = (\mathbf{v}_i^h, \mathbf{f})_{\Omega} \qquad \forall \{\mathbf{v}_i^h, q_i^h\} \in \mathcal{V}_{\mathbf{u}p}^h. \tag{2.5}$$

The semi-linear form $B_{\mathrm{NS}}^{\mathrm{FV}}\left(\mathbf{v}_i^h, q_i^h; \mathbf{u}^h, p^h\right)$ on the left hand side of (2.5) is obtained from (2.2) after applying Gauss' theorem to the convective term, to the pressure term, to the viscous term, and to the continuity term as

$$B_{\mathrm{NS}}^{\mathrm{FV}}\left(\mathbf{v}_i^h, q_i^h; \mathbf{u}^h, p^h\right) = \left(\mathbf{v}_i^h, \frac{\partial \mathbf{u}^h}{\partial t}\right)_\Omega + \left(\mathbf{v}_i^h, \left(\mathbf{u}^h \otimes \mathbf{u}^h\right) \cdot \mathbf{n}\right)_{\Gamma_i} + \left(\mathbf{v}_i^h, p^h \mathbf{n}\right)_{\Gamma_i}$$
$$- \left(\mathbf{v}_i^h, \nu\left(\nabla \mathbf{u}^h\right) \cdot \mathbf{n}\right)_{\Gamma_i} + \left(q_i^h, \mathbf{u}^h \cdot \mathbf{n}\right)_{\Gamma_i}. \tag{2.6}$$

In (2.6), $\mathbf{n}$ indicates the respective outward normal vector of unit length to Γ_i, where Γ_i denotes the boundary of the support of $\mathbf{v}_i^h$ and q_i^h, respectively.

The characteristic length scale h chosen in large eddy simulations is usually considerably larger than the smallest length scale of the problem under investigation. In no way can all scales of the problem be resolved. Therefore, the subgrid viscosity approach, a standard way of taking into account the (dissipative) effect of unresolved scales in the traditional LES, is applied. According to this, a subgrid viscosity term is added to (2.5), resulting in

$$B_{\mathrm{NS}}^{\mathrm{FV}}\left(\mathbf{v}_i^h, q_i^h; \mathbf{u}^h, p^h\right) - \left(\mathbf{v}_i^h, \nu_{\mathrm{T}}\left(\nabla \mathbf{u}^h\right) \cdot \mathbf{n}\right)_{\Gamma_i} = \left(\mathbf{v}_i^h, \mathbf{f}\right)_\Omega, \tag{2.7}$$

where ν_{T} denotes the subgrid viscosity. Note that the subgrid viscosity term is added to all resolved scales of the problem in (2.7). Note also that the reason for introducing a model term in this context is mathematically different from the usual necessity of introducing a model term due to the appearance of a subfilter-scale or a subgrid-scale stress tensor in the strong formulation of the Navier-Stokes equations in a traditional LES. Nevertheless, the physical necessity of accounting for the missing effect of unresolved scales on the resolved scales is the same in both the traditional and the variational multiscale LES.

3. Separation of scales and multiscale formulation

The resolved velocity vector $\mathbf{u}^h$ is separated into a large-scale part and a small-scale part subject to

$$\mathbf{u}^h = \left(\overline{\mathbf{u}} + \mathbf{u}'\right)^h. \tag{3.1}$$

With respect to this complete resolution level, a large-scale resolution level is identified *a priori*. This level is characterized by the control volume length $\overline{h}$, where $\overline{h} > h$ and accordingly yields a large-scale velocity $\overline{\mathbf{u}}^{\overline{h}}$. The small-scale velocity is consistently defined on the complete resolution level, characterized by the length h, as

$$\mathbf{u}'^h = \mathbf{u}^h - \overline{\mathbf{u}}^h, \tag{3.2}$$

where $\overline{\mathbf{u}}^h$ denotes the large-scale value transfered to this level. The scale separation used in the present study relies on multigrid operators. At the outset of the numerical simulation, two grids are created: a coarser grid, which is called the "parent" grid, and a finer grid, which is called the "child" grid. The child grid is obtained by an isotropic hierarchical subdivision of the parent grid. In the simulations of the present study, a subdivision by a factor of two in each spatial direction is exclusively applied. For more details concerning the implementation, refer to Gravemeier (2005a).

The general class of scale-separating operators based on multigrid operators is formulated as

$$\overline{\mathbf{u}}^h = S^{\mathrm{m}}\left[\mathbf{u}^h\right] = P \circ R\left[\mathbf{u}^h\right] = P\left[\overline{\mathbf{u}}^{\overline{h}}\right], \tag{3.3}$$

where the multigrid scale-separating operator S^{m} consists of the sequential application of

a restriction operator R and a prolongation operator P. Applying the restriction operator on $\mathbf{u}^h$ yields a large-scale velocity $\overline{\mathbf{u}}^{\overline{h}}$ defined at the degrees of freedom of the parent grid, which is then prolongated, in order to obtain a large-scale velocity $\overline{\mathbf{u}}^h$ defined at the degrees of freedom of the child grid. Various restriction as well as prolongation operators may be used in (3.3). Two special combinations of restriction and prolongation operators were analyzed in Gravemeier (2005a) and were compared to discrete smooth filters, which are widely used in traditional LES. It was shown that these two multigrid scale-separating operators represent computationally efficient methods for separating the resolved scales of the problem in comparison with discrete smooth filters. Both multigrid scale-separating operators rely on the same restriction operator but apply different prolongation operators afterwards.

The restriction operator is defined as a volume-weighted average over all child control volumes within one parent control volume subject to

$$\overline{\mathbf{u}}_j^{\overline{h}} = \frac{\sum\limits_{i=1}^{n_{\mathrm{cop}}} |\Omega_i| \, \mathbf{u}_i^h}{\sum\limits_{i=1}^{n_{\mathrm{cop}}} |\Omega_i|}, \tag{3.4}$$

where $\overline{\mathbf{u}}_j^{\overline{h}}$ denotes the large-scale velocity at the center of the parent control volume $\overline{\Omega}_j$, and n_{cop} denotes the number of child control volumes in $\overline{\Omega}_j$. The first prolongation operator P^{p} yields a constant prolongation, which is given as

$$\overline{\mathbf{u}}_i^h = P^{\mathrm{p}} \left[\overline{\mathbf{u}}_j^{\overline{h}} \right]_i = \overline{\mathbf{u}}_j^{\overline{h}} \qquad \forall \, \Omega_i \subset \overline{\Omega}_j \tag{3.5}$$

and zero elsewhere. It was shown in Gravemeier (2005a) that the scale-separating operator defined as

$$S^{\mathrm{pm}} := P^{\mathrm{p}} \circ R \tag{3.6}$$

has the property of a projector, which is indicated by the additional superscript "p". The projector (3.6) is the same operator used in Koobus & Farhat (2004), although in that study it was not derived from the general formulation (3.3) and was therefore not split into a restriction and prolongation operator.

The second prolongation operator considered in the present study yields a linear prolongation subject to

$$\overline{\mathbf{u}}_i^h = P^{\mathrm{s}} \left[\overline{\mathbf{u}}_j^{\overline{h}} \right]_i = \overline{\mathbf{u}}_j^{\overline{h}} + \left(\nabla^{\overline{h}} \overline{\mathbf{u}}_j^{\overline{h}} \right) \cdot (\mathbf{r}_i - \overline{\mathbf{r}}_j) \qquad \forall \, \Omega_i \subset \overline{\Omega}_j \tag{3.7}$$

and zero elsewhere. The vectors $\mathbf{r}_i$ and $\overline{\mathbf{r}}_j$ denote geometrical vectors pointing to the centers of the child control volume Ω_i and of the parent control volume $\overline{\Omega}_j$, respectively. The operator $\nabla^{\overline{h}}$ describes the discrete gradient operator on the parent grid. Due to this, values from neighboring parent control volumes and, consequently, from child control volumes contained in these neighboring parent control volumes influence the final large-scale value in the child control volume Ω_i. The prolongation P^{s} does not provide us with a projective scale-separating operation. Rather, it produces a smoothing prolongation, which is, at least, smoother than the prolongation produced by P^{p}. Thus, it is indicated by the additional superscript "s", and the complete scale-separating operator is defined as

$$S^{\mathrm{sm}} := P^{\mathrm{s}} \circ R. \tag{3.8}$$

For the actual scale separation within a variational finite volume formulation, a large-scale velocity weighting function given as

$$\overline{\mathbf{v}}^h = \sum_i \overline{\mathbf{v}}_i^h, \tag{3.9}$$

where

$$\overline{\mathbf{v}}_i^h = \mathbf{1} \qquad \text{in} \quad \overline{\Omega}_i \tag{3.10}$$

and zero elsewhere, is introduced analogous to the large-scale velocity solution function. $\overline{\Omega}_i$ denotes the i-th control volume of the discretization with the characteristic control volume length $\overline{h}$. The separation of the weighting functions enables a decomposition of the variational equation (2.5) into a large- and a small-scale equation. The coupled system of large- and small-scale equations, which results from an initial three-scale separation, may be found, for instance, in Gravemeier (2005b). For the particular scale separation used in the present work, these two equations may eventually be reunified to *one* final equation; see Gravemeier (2005b). In this final equation, the scale separation based on S^{m} remains perceptible only with respect to the subgrid viscosity term. Based on the variational finite volume formulation (2.7), the following problem statement for each $\mathbf{v}_i^h$, q_i^h, and $\overline{\mathbf{v}}_i^h$, where the child grid control volume Ω_i is contained in the parent grid control volume $\overline{\Omega}_i$, is obtained: find $\{\mathbf{u}^h, p^h\} \in \mathcal{S}_{\mathbf{u}p}^h$, such that

$$
\begin{aligned}
&B_{\mathrm{NS}}^{\mathrm{FV}}\left(\mathbf{v}_i^h, q_i^h; \mathbf{u}^h, p^h\right) - \left(\mathbf{v}_i'^h, \nu_{\mathrm{T}}'\left(\nabla \mathbf{u}'^h\right)\cdot\mathbf{n}\right)_{\Gamma_i'} \\
&= B_{\mathrm{NS}}^{\mathrm{FV}}\left(\mathbf{v}_i^h, q_i^h; \mathbf{u}^h, p^h\right) - \left(\mathbf{v}_i^h, \nu_{\mathrm{T}}'\left(\nabla\left(\mathbf{u}^h - \overline{\mathbf{u}}^h\right)\right)\cdot\mathbf{n}\right)_{\Gamma_i} + \left(\overline{\mathbf{v}}_i^h, \nu_{\mathrm{T}}'\left(\nabla\left(\mathbf{u}^h - \overline{\mathbf{u}}^h\right)\right)\cdot\mathbf{n}\right)_{\overline{\Gamma}_i} \\
&= B_{\mathrm{NS}}^{\mathrm{FV}}\left(\mathbf{v}_i^h, q_i^h; \mathbf{u}^h, p^h\right) \\
&\quad - \left(\mathbf{v}_i^h, \nu_{\mathrm{T}}'\left(\left(\nabla\mathbf{u}^h\right)\cdot\mathbf{n} - \left(\nabla\overline{\mathbf{u}}^h\right)\cdot\mathbf{n}\right)\right)_{\Gamma_i} + \left(\overline{\mathbf{v}}_i^h, \nu_{\mathrm{T}}'\left(\left(\nabla\mathbf{u}^h\right)\cdot\mathbf{n} - \left(\nabla\overline{\mathbf{u}}^h\right)\cdot\mathbf{n}\right)\right)_{\overline{\Gamma}_i} \\
&= \left(\mathbf{v}_i^h, \mathbf{f}\right)_\Omega, \tag{3.11}
\end{aligned}
$$

where $\mathbf{v}'^h$ denotes the small-scale part of the velocity weighting function and ν_{T}' the subgrid viscosity depending on the small resolved scales, to be defined below. The boundary Γ_i is split up into a large-scale boundary $\overline{\Gamma}_i$ and accordingly, a small-scale boundary subject to

$$\Gamma_i' = \Gamma_i - \overline{\Gamma}_i. \tag{3.12}$$

For one of the scale-separating operators (i.e., S^{pm}), a further simplification of (3.11) is possible. A crucial difference between S^{pm} and S^{sm} consists of the fact that there is no large-scale (subgrid) viscous flux for S^{pm} across the small-scale boundary subject to (3.12). As a result, (3.11) may be specified for S^{pm} as

$$B_{\mathrm{NS}}^{\mathrm{FV}}\left(\mathbf{v}_i^h, q_i^h; \mathbf{u}^h, p^h\right) - \left(\mathbf{v}_i'^h, \nu_{\mathrm{T}}'\left(\nabla\mathbf{u}^h\right)\cdot\mathbf{n}\right)_{\Gamma_i'} = \left(\mathbf{v}_i^h, \mathbf{f}\right)_\Omega, \tag{3.13}$$

since it is guaranteed by the definition of S^{pm} that $\left(\nabla\overline{\mathbf{u}}^h\right)\cdot\mathbf{n} = 0$ and, hence, $\left(\nabla\mathbf{u}^h\right)\cdot\mathbf{n} = \left(\nabla\mathbf{u}'^h\right)\cdot\mathbf{n}$ on Γ_i'. The validity of (3.13) for S^{pm} in the finite volume method provides substantial computational savings in contrast to S^{sm}. All calls of the scale-separating computational subroutine during the actual solution procedure (e.g. at the beginning of each solver iteration step for determining the updated large-scale velocity field for the residual calculation) are not required for S^{pm}. Note that in both (3.11) and (3.13) the subgrid viscosity term directly acts only on the small resolved scales, in contrast to

(2.7). The indirect influence on the large resolved scales, however, is ensured due to the inherent coupling of the large and small resolved scales.

4. Subgrid-scale modeling

Two different versions of the Smagorinsky model are used for the calculation of the subgrid viscosity ν_{T} and ν'_{T}, respectively. The subgrid viscosity ν_{T} is given as

$$\nu_{\mathrm{T}} = (C_{\mathrm{S}}h)^2 \left| \varepsilon \left(\mathbf{u}^h \right) \right|, \qquad (4.1)$$

where ε denotes the rate-of-deformation tensor and depends on the complete resolved velocity $\mathbf{u}^h$, and C_{S} denotes the Smagorinsky model constant. In the case of ν'_{T}, the dependence is restricted to the small-scale part of the velocity as

$$\nu_{\mathrm{T}} = (C_{\mathrm{S}}h)^2 \left| \varepsilon \left(\mathbf{u}'^h \right) \right| = (C_{\mathrm{S}}h)^2 \left| \varepsilon \left(\mathbf{u}^h - \overline{\mathbf{u}}^h \right) \right|. \qquad (4.2)$$

The actual evaluation of (4.1) or (4.2) is performed in every child control volume Ω_i so that a value $\nu_{\mathrm{T},i}$ or $\nu'_{\mathrm{T},i}$, respectively, in every child control volume is obtained. The characteristic length scale of the child control volume Ω_i is assumed to be the cube root of the respective measure, that is,
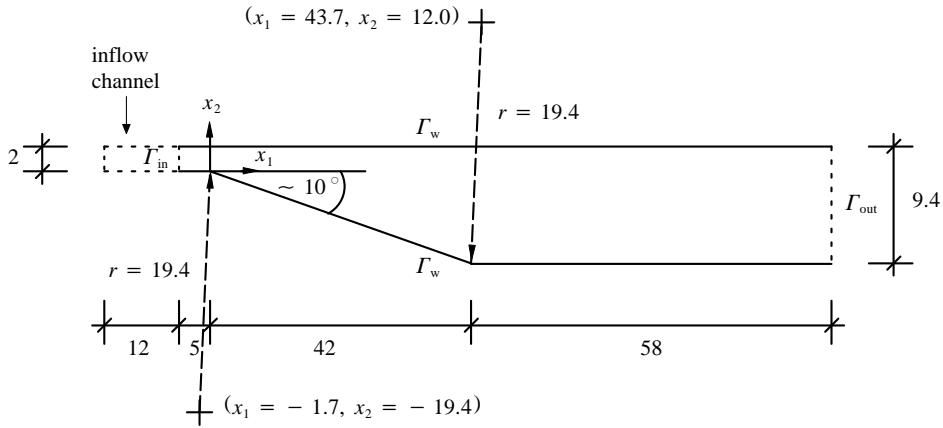
$$h_i = |\Omega_i|^{\frac{1}{3}}. \qquad (4.3)$$

The choice of the constant C_{S} in the case of turbulent flow in a diffuser is not an easy one, since there appears to be a complete lack of available data for this case. For the channel flow simulations in Gravemeier (2005a), the constant was chosen to be 0.1. This choice is maintained for the simulations of the inflow channel to the diffuser. For the actual diffuser, a value of $C_{\mathrm{S}} = 0.18$ is applied. It represents the value obtained in Lilly's analysis (see, for example, Lilly (1967)), thereby balancing turbulent kinetic energy production and dissipation, but it has mainly been applied for homogeneous isotropic turbulence. However, this choice is supported by a simple comparison of values observed during dynamic calculations in the inflow channel and in the diffuser. Considering a volume-averaged value of C_{S} over the respective domain, values of approximately 0.15 and 0.25 are obtained in the inflow channel and in the diffuser, respectively (a ratio of about 0.6). Setting 0.1 in this ratio, a constant $C_{\mathrm{S}} \approx 0.17$ can be calculated for the diffuser based on this rough approximation, which is close to the chosen value 0.18.

In order to actually calculate C_{S} as a model parameter, the dynamic modeling procedure is applied as proposed in Germano *et al.* (1991), which enables a computation of C_{S} as a function of time and position. The procedure was adapted in Gravemeier (2005a) to the particular scale separation used in the present work, where it is discussed in fuller detail. In order to account for potential numerical problems related to negative values of C_{S}, a special clipping proposed in Mahesh *et al.* (2002) is performed.

5. Numerical results

The diffuser geometry, which basically matches the experimental configuration in Buice & Eaton (1997) and in Obi *et al.* (1993), as well as the numerical setup in Kaltenbach *et al.* (1999) and in Wu *et al.* (2006), is shown in Fig. 1 in the x_1-x_2-plane. The inlet plane is located at $x_1 = -5$, followed by an inlet channel of length $5\delta_c$, where the inlet channel half-width δ_c is set to be of unit length. The latter inlet channel half-width δ_c matches that of the preceding inflow channel. The asymmetric diffuser of length $42\delta_c$ opens with

$(x_1 = 43.7, \ x_2 = 12.0)$

inflow channel

x_2

Γ_w

$r = 19.4$

2

Γ_in

x_1

$\sim 10\,^{\circ}$

Γ_out 9.4

$r = 19.4$

Γ_w

12 5 42 58

$(x_1 = -1.7, \ x_2 = -19.4)$

FIGURE 1. Diffuser geometry in x_1-x_2-plane

an angle of 10°. This corresponds to an expansion ratio of $h_\mathrm{in}/h_\mathrm{out} = 4.7$. It is followed by an outlet channel of height $9.4\delta_\mathrm{c}$ and length of approximately $58\delta_\mathrm{c}$, which locates the outlet plane at about $x_1 = 100$. The outlet channel length matches the one in Wu *et al.* (2006) and is considerably longer than the one in Kaltenbach *et al.* (1999). Due to the relatively long distance between the last point of measurement and the outlet plane, any significant upstream influence of the outlet plane is minimized. Nevertheless, the recovery into a canonical channel flow will not be reached even within this longer outlet channel. See Buice & Eaton (1997) and Kaltenbach *et al.* (1999). Both the upstream corner at $x_1 = 0$ and the downstream corner at $x_1 = 42$ are rounded with a radius of $r = 19.4$, where the curvature centers are located as shown in Fig. 1. The length of the domain in x_3-direction (i.e. orthogonal to the depiction in Fig. 1) is chosen to be $8\delta_\mathrm{c}$, which matches the spanwise length in Wu *et al.* (2006) and represents the largest value for the spanwise length investigated in Kaltenbach *et al.* (1999). The inflow channel, in which the inflow velocity $\mathbf{u}^\mathrm{in}(t)$ (i.e. the unsteady Dirichlet boundary condition at the inflow boundary Γ_in) is generated, matches the inlet channel in its dimensions in x_2- and x_3-direction. According to Wu *et al.* (2006), an inflow channel length of $12\delta_\mathrm{c}$ is chosen. No-slip boundary conditions are assumed at the upper and lower walls Γ_w of the diffuser, a convective boundary condition is prescribed at the outflow boundary Γ_out, and periodic boundary conditions are assumed on the boundaries Γ_per in x_3-direction (i.e. this periodicity is assumed orthogonal to the depiction in Fig. 1).

The diffuser, including inlet and outlet channel, is discretized using 290, 64, and 80 control volumes in x_1-, x_2-, and x_3-direction, respectively. The respective parent grid contains 145, 32, and 40 control volumes in x_1-, x_2-, and x_3-direction, respectively. The control volumes are uniformly distributed in the spanwise direction. In the wall-normal direction, a cosine function for refinement towards the walls for the parent grid is used, with the isotropic hierarchical subdivision procedure subsequently applied. In the streamwise direction, the following control volume distribution is employed: in the inlet channel, h_1 decreases linearly from 0.15 to 0.05 in the asymmetric diffuser section, h_1 increases linearly from 0.05 to 0.475, in the first section of the outlet channel (ranging from $x_1 = 42$ to $x_1 = 74.5$), h_1 increases linearly from 0.475 to 0.825, and in the remaining section of the outlet channel, the control volumes are uniformly distributed with $h_1 = 0.825$. Comparing the discretization of the diffuser to the finer discretization in Wu *et al.* (2006), which employed 590, 100, and 110 control volumes in x_1-, x_2-, and x_3-direction, it is

stated that less than 23% of the total number of control volumes are used in the present case. The time step δt is fixed to be 0.002, starting from a zero velocity field as the initial condition for the velocity. More details concerning the numerical setup can be found in Gravemeier (2005c). All numerical simulations are conducted using the CDP-α code; see, for example, Ham *et al.* (2003) for details of the code.

As in Gravemeier (2005a), three different methods are investigated:

i) The dynamic Smagorinsky (DS) model in a non-multiscale application subject to (2.7), with the subgrid viscosity subject to (4.1)

ii) The constant-coefficient-based Smagorinsky model within the multiscale environment (CMS) subject to (3.11) or (3.13), respectively, with the subgrid viscosity subject to (4.2)

iii) The dynamic Smagorinsky model within the multiscale environment (DMS) subject to (3.11) or (3.13), respectively, with the subgrid viscosity subject to (4.2).

All of these methods are analyzed for the scale-separating operator S^{pm}. In the following diagrams, the abbreviation DMS-PM, for instance, indicates the variational multiscale LES incorporating a dynamic Smagorinsky model, with the scale-separating operator S^{pm} applied. The scale-separating operator S^{sm} is only investigated for CMS, since this method revealed the most notable differences between the scale-separating operators for the test case in Gravemeier (2005a). Results are also reported for simulations using no model at all (NM), which represents a coarse (i.e., not sufficiently resolved) DNS. Based on evaluations in Gravemeier (2005a), the characteristic length scale ratio for the DS- and DMS-simulations using S^{pm} is set to 2.5. The Wu-LES, to which the results are compared, applies the same dynamic Smagorinsky model in a traditional non-multiscale LES (i.e. DS), including the same special clipping according to Mahesh *et al.* (2002). However, the differences in the DS method used in the present study refer to, on the one hand, the fact that the Wu-LES used traditional discrete smooth filters instead of the multigrid scale-separating operators for dynamic modeling. On the other hand, the discretization, both in terms of the number of control volumes and in the generation of the grid, is different, as outlined above.

Evaluating the necessary computational effort provides the following numbers. Setting the computational effort for NM to 1.0, the relative measures for CMS-PM, CMS-SM, DS-PM and DMS-PM are approximately 1.08, 1.34, 1.27, and 1.32, respectively. These numbers are even more impressively in favor of CMS-PM than the ones for the channel in Gravemeier (2005a). Thus, it is confirmed that CMS in combination with PM is a very computationally efficient method. In the present case, it is substantially more efficient than, for instance, DS. Using the scale-separating operator SM, the numbers increase drastically for CMS. Less effort is required for PM than for SM because of the opportunity to use (3.13) in preference to (3.11), which obviates the execution of a potential scale-separating operation at the beginning of each iteration within the SOR solver, as mentioned in section 3.

Figure 2 depicts the results for the skin friction coefficient along the upper wall of the diffuser. It is apparent that all methods tend to under-predict C_{f} compared to the results from the Wu-LES and from the Buice-experiment. The worst results are produced by CMS-SM. The profile for NM is closest to the ones from the Wu-LES and the Buice-experiment immediately behind the diffuser throat, but it gets worse in its prediction further downstream. DS-PM yields a fairly good prediction throughout the diffuser, and DMS-PM produces worse results than DS-PM. The prediction produced by CMS-PM is the best overall. It is the only method yielding results that almost match the experimental
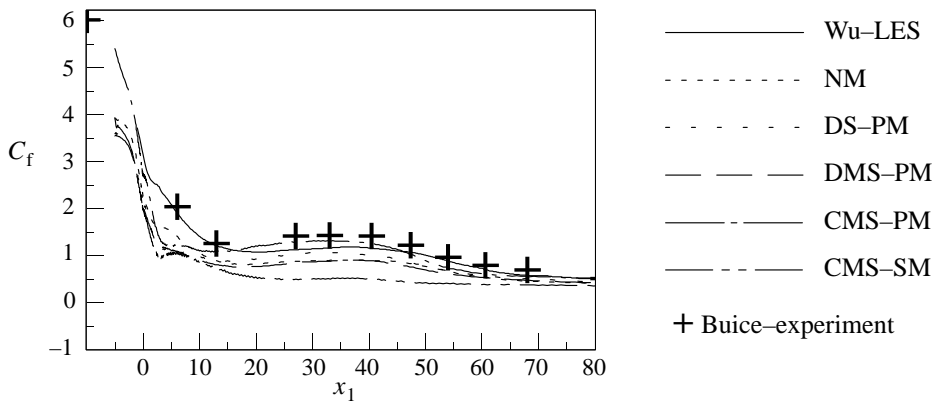
FIGURE 2. Skin friction coefficient (factor 1000) along the upper wall of the diffuser

results in the section of the diffuser between $x_1 \approx 18$ and $x_1 \approx 46$ at the upper wall. In this part of the diffuser, which is approximately the region in which the flow is separated, as will be seen below, CMS-PM appears to produce even better results than the more finely discretized Wu-LES. Furthermore, it seems to be the only one of the present methods that would have been able to predict the first point from the Buice-experiment at $x_1 \approx -10$, if the inlet channel had been elongated.

In Figs. 3-6, the profiles for the mean streamwise velocity at four locations along the diffuser are displayed. Behind the entry to the asymmetric diffuser section, all methods predict a velocity profile that is in qualitative agreement with the ones from the Wu-LES and the Obi-experiment, although all of them under-predict the maximum velocity (see Fig. 3). The best prediction is produced by CMS-PM, followed by DS-PM, DMS-PM, CMS-SM, and NM in descending order of their quality of approximation. CMS-PM even appears to under-predict the experimental data by approximately the same amount as the Wu-LES over-predicts it. The second location depicted in Fig. 4 is slightly more than halfway down the diffuser, and the flow separation, which should be expected at $x_1 \approx 16$ according to the Buice-experiment, has already taken place. By observing Fig. 4 as well as Figs. 5-6, it is apparent that CMS-SM is inadequate, since it is the only method that fails to predict the flow separation. The best approximation of the results from the Obi-experiment in Fig. 4 is provided by CMS-PM and the second best by DS-PM, as both are even closer to the experimental data than is the Wu-LES towards the lower wall. Compared to the experimental data, the Wu-LES does not predict the separation point as accurately as does CMS-PM and DS-PM. At the next location further downstream depicted in Fig. 5, CMS-PM almost matches the experimental data in the lower part of the diffuser, predicting the reversed flow very accurately. In the outlet channel, this very good approximation cannot be completely maintained (see Fig. 6). DMS-PM is less accurate at all three locations shown in Figs. 4-6. Aside from CMS-SM, NM produces the worst prediction, with the exception of Fig. 5 (i.e. close to the end of the asymmetric diffuser section), where it is at least slightly better than DMS-PM. However, the most obvious failure of NM is its clear overestimation of the recirculating velocity in the outlet channel. Thus, it does not provide a reasonable approximation of the flow separation as well as of the reattachment point, which should be expected at $x_1 \approx 52$, according to the Buice-experiment.

V. Gravemeier
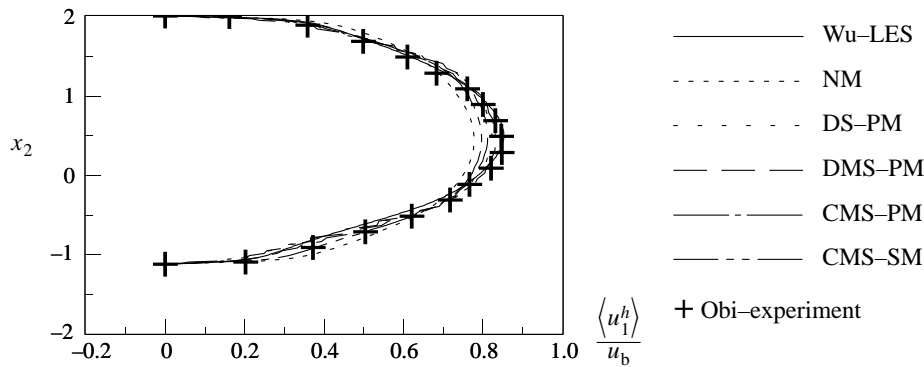
FIGURE 3. Mean streamwise velocity at $x_1 = 6.4$
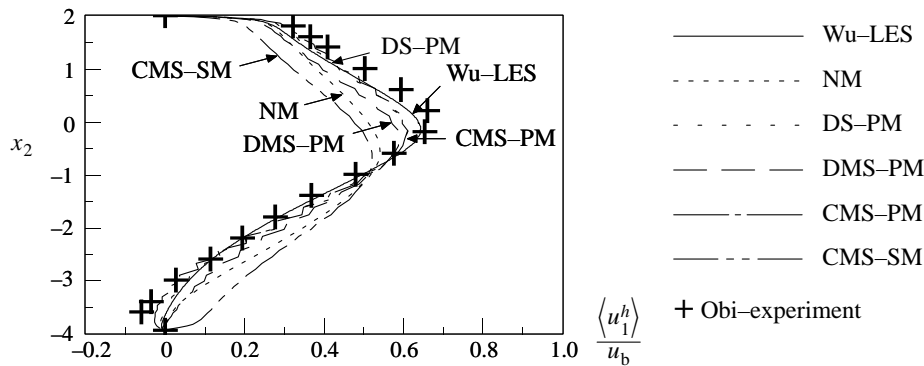
FIGURE 4. Mean streamwise velocity at $x_1 = 22.4$
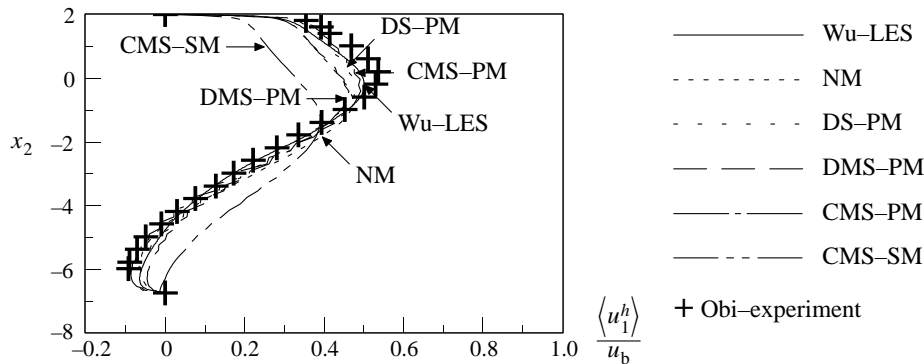
FIGURE 5. Mean streamwise velocity at $x_1 = 38.4$

6. Conclusions

Variational multiscale large eddy simulation has been applied to turbulent flow in a diffuser. Turbulent flow in a diffuser represents a challenging test case, in particular due to the appearance of flow separation, which is caused by an adverse pressure gradient, and subsequent reattachment. Two different scale-separating operators based on multigrid operators, which are applicable within both a finite element and a finite volume method, have been used for separating large resolved scales and small resolved
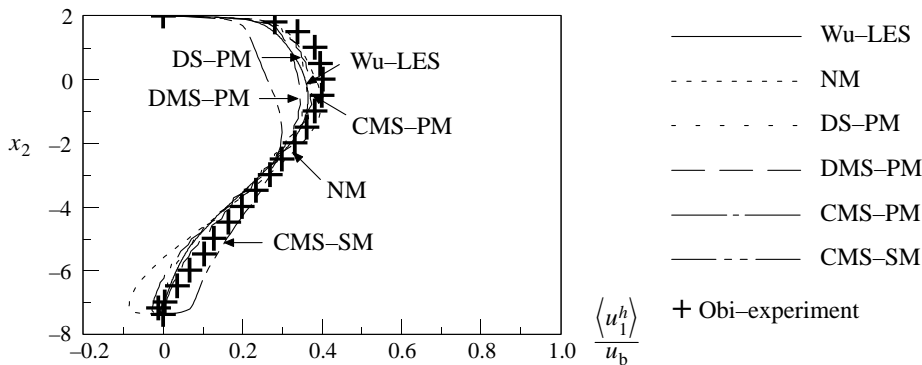
FIGURE 6. Mean streamwise velocity at $x_1 = 58.4$

scales. Dynamic as well as constant-coefficient-based subgrid-scale modeling has been employed within the variational multiscale LES. All approaches have been implemented in a second-order energy-conserving finite volume method particularly suited for applications on hybrid unstructured grids in complex geometries. The results obtained by the various approaches have been compared to results from a recent non-multiscale LES with dynamic subgrid-scale modeling performed on an approximately 5 times finer grid and experimental results.

The results have led to the following conclusions. For results not shown in this Brief, see Gravemeier (2005c).

• The constant-coefficient-based variational multiscale LES using the projective scale-separating operator (CMS-PM) produces the most accurate results for the wall static pressure coefficient and for the skin friction coefficient along the diffuser, as well as for the mean velocity in streamwise direction and the root-mean-square velocity in wall-normal direction. Within the flow separation region, CMS-PM provides even better predictions of the skin friction coefficient and the mean streamwise velocity than does a traditional LES on a considerably finer grid.

• CMS-PM and non-multiscale LES with dynamic subgrid-scale modeling (DS-PM) yield the most accurate results for the root-mean-square velocity in streamwise direction, both being of similar accuracy overall for these values.

• The constant-coefficient-based variational multiscale LES using the smoothing, non-projective scale-separating operator (CMS-SM) fails to predict the flow separation and reattachment at the lower wall. As a result, this scale-separating operator should be disqualified from further use.

• The variational multiscale LES with dynamic subgrid-scale modeling using the projective scale-separating operator (DMS-PM) produces worse predictions than does DS-PM for almost all investigated values.

• Computationally, CMS-PM is by far the most efficient of all approaches considered in the present study. In particular, it reduces the computing time by about 18% compared to DS-PM. This is an even larger reduction compared to the channel flow simulations in Gravemeier (2005a), where the computing time was reduced by about 5%.

Acknowledgments

Wu for providing the results from his recent LES study of the diffuser, and for helpful discussions regarding the diffuser simulations. The author is also grateful to Parviz Moin and Gregory Burton for helpful discussions.

REFERENCES

BUICE, C. U. & EATON, J. K. 1997 Experimental investigation of flow through an asymmetric plane diffuser. *TSD-107*, Department of Mechanical Engineering, Stanford University.

GERMANO, M., PIOMELLI, U., MOIN, P. & CABOT, W. H. 1991 A dynamic subgrid-scale eddy vicosity model. *Phys. Fluids* **3**, 1760-1765.

GRAVEMEIER, V. 2005a Scale-separating operators for variational multiscale large eddy simulation of turbulent flows. *J. Comp. Phys.*, **212**, 400-435.

GRAVEMEIER, V. 2005b The variational multiscale method for laminar and turbulent flow. *Arch. Comput. Meth. Engrg.*, in press.

GRAVEMEIER, V. 2005c Variational multiscale large eddy simulation of turbulent flow in a diffuser. *Preprint.*

HAM, F., APTE, S., IACCARINO, G., WU, X., HERRMANN, M., CONSTANTINESCU, G., MAHESH, K. & MOIN, P. 2003 Unstructured LES of reacting multiphase flows in realistic gas turbine combustors. *Annual Research Briefs 2003*, Center for Turbulence Research, NASA Ames/Stanford Univ., 139-160.

HELLSTEN, A. & RAUTAHEIMO, P. (EDS.) 1999 Proceedings of the 8th ERCOFTAC/IAHR/COST workshop on refined turbulence modeling, Helsinki University of Technology, Espoo, Finland, June 17-18.

HUGHES, T. J. R., MAZZEI, L. & JANSEN, K. E. 2000 Large eddy simulation and the variational multiscale method. *Comput. Visual. Sci.* **3**, 47-59.

KALTENBACH, H.-J., FATICA, M., MITTAL, R., LUND, T. S. & MOIN, P. 1999 Study of flow in a planar asymmetric diffuser using large eddy simulation. *J. Fluid Mech.* **390**, 151-185.

KOOBUS, B. & FARHAT, C. 2004 A variational multiscale method for the large eddy simulation of compressible turbulent flows on unstructured meshes - application to vortex shedding. *Comput. Methods Appl. Mech. Engrg.* **193**, 1367-1383.

LILLY, D. K. 1967 The representation of small-scale turbulence in numerical simulation experiments, Proceedings of the IBM Scientific Computing Symposium on Environmental Sciences, Yorktown Heights, New York.

MAHESH, K., CONSTANTINESCU, G., APTE, S., IACCARINO, G., HAM, F. & MOIN, P. 2002 Progress towards large-eddy simulation of turbulent reacting and non-reacting flows in complex geometries. *Annual Research Briefs 2002*, Center for Turbulence Research, NASA Ames/Stanford Univ., 115-142.

OBI, S., AOKI, K. & MASUDA, S. 1993 Experimental and computational study of turbulent separating flow in an asymmetric plane diffuser, *Ninth Symp. on Turbulent Shear Flows*, Kyoto, Japan, August 16-19.

WU, X., SCHLUETER, J., MOIN, P., PITSCH, H., IACCARINO, G. & HAM, F. 2006 Computational study on the internal layer in a diffuser. *J. Fluid Mech.*, in press.